Synthesis and transport properties of p-type lead-free AgSn$_m$SbSe$_2$Te$_m$ thermoelectric systems

Sebastián Figueroa-Millon [a], Inmaculada Álvarez-Serrano [b], David Bérardan [c], Antonio Galdámez [a, *]

[a] Departamento de Química, Facultad de Ciencias, Universidad de Chile, Santiago, Chile
[b] Departamento de Química Inorgánica I, Facultad de Ciencias Químicas, Universidad Complutense de Madrid, 28040, Madrid, Spain
[c] SP2M — ICMMO (UMR CNRS 8182), Univ. Paris-Sud, Univ. Paris-Saclay, F-91405, Orsay, France

HIGHLIGHTS

- p-type AgSn$_m$SbSe$_2$Te$_m$ systems exhibit typical degenerate semi-conductor behavior.
- The maximum $S^2\sigma$ value of $22\,\mu\mathrm{W\,cm^{-1}\,K^{-2}}$ was obtained for AgSn$_2$SbSe$_2$Te$_2$ SPSed-sample.
- ZT values of ~0.10 were obtained at room temperature.
- κ_{latt} of AgSn$_m$SbSe$_2$Te$_m$ systems was ~0.6 W m^{-1} K^{-1}.

GRAPHICAL ABSTRACT
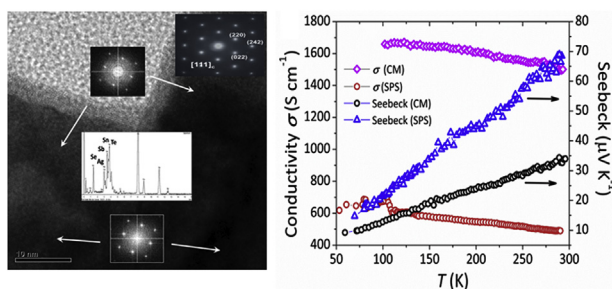
ABSTRACT

We report the synthesis, characterization and thermoelectric properties of lead-free AgSn$_m$SbSe$_2$Te$_m$ ($m = 2$ and 10) systems. Powder X-ray diffraction patterns and Rietveld refinement results were consistent with phases belonging to the $Pm\overline{3}m$ space group. The microstructures and morphologies of these systems were investigated using scanning electron microcopy (SEM) and high-resolution transmission electron microscopy (HRTEM). Parallelepiped bars for transport measurements were prepared using two methods: the classical method (CM) from melted samples and the spark plasma sintering (SPS). The AgSn$_m$SbSe$_2$Te$_m$ ($m = 2$ and 10) systems exhibited typical degenerate semiconductor behavior, with a carrier concentration of approximately $+10^{21}\,\mathrm{cm^{-3}}$. We determined that the Seebeck coefficient can be substantially increased from approximately $+40\,\mu\mathrm{V\,K^{-1}}$ (CM) to $+70\,\mu\mathrm{V\,K^{-1}}$ (SPS) in AgSn$_2$Sb-Se$_2$Te$_2$ at room temperature. Consequently, the power factor ($S^2\sigma$) was ~22 $\mu\mathrm{W\,cm^{-1}\,K^{-2}}$. On the basis of the electrical and thermal transport properties, ZT values of ~0.10 were obtained at room temperature.

© 2018 Elsevier B.V. All rights reserved.

1. Introduction

The emerging global demand for energy production has intensified the interest in more effective power generation methods. The need for energy sources other than fossil fuels has motivated research on new materials that can be used to exploit various renewable energy sources, such as solar energy, wind, and biomass. Thermoelectric materials can be employed in energy-conversion devices that serve a primary role in global sustainable power generation [1—5].

Candidates for materials that exhibit thermoelectric behavior at moderate temperatures include $AgPb_mSbTe_{2+m}$, which is often abbreviated as LAST (lead, antimony, silver, tin, tellurium)-m, and $Ag(Pb_{1-y}Sn_y)Pb_mSbTe_{2+m}$, which is often abbreviated as LASTT (lead, antimony, silver tin, tellurium)-m [6–13]. These chalcogenides adopt the same crystal structure as bulk PbTe (NaCl-type lattice). Through a combination of a power-factor enhancement and a strong reduction in thermal conductivity, large values of the figure of merit $ZT = S^2\sigma/\kappa_{tot}$ in LAST-m systems ($S^2\sigma \sim 34\,\mu W\,cm^{-1}\,K^{-2}$ in LAST-18) have been observed [7–9]. LAST-m and LASTT-m systems exhibit p-type semiconductor behavior. Electrical transport studies have shown that the thermoelectric properties of this system can be fine-tuned via two compositional parameters: the Pb/Sn ratio and the $AgSbTe_2$ chemical composition. Another example of an excellent p-type PbTe-based material is $(PbTe)_m$-$Na_{1-x}Sb_yTe_2$ SALT (sodium, antimony, silver, tin, tellurium)-m [14]. In this system, Na^+ ions have the same oxidation state as the Ag^+ ions in LAST-m. For fixed values of y and m in $(PbTe)_m$-$Na_{1-x}Sb_yTe_2$, the electrical conductivity is a function of the temperature, $\sigma \sim T^{-n}$. The power factor ($S^2\sigma$) varies as an approximately linear function of y.

High-resolution transmission electron microscopy (HRTEM), Electron diffraction and EDS microanalysis have shown Ag-Sb-rich nanostructures embedded in a PbTe lattice in $(PbTe)_m$-$AgSbTe_2$ (LAST-m) systems. These nanostructures are considered to be responsible for substantially reducing the thermal conductivity by increasing the scattering of the short wavelength phonons at the interfaces [9,13]. In SALT-m systems, HRTEM investigation revealed Na-Sb-rich and Pb-rich clusters in the lattice [14]. Therefore, the electronic behavior of these systems is highly sensitive to the microstructural arrangements, as the formation of these clusters both influences the main scattering process of the charge carriers and possibly their concentration.

ZT values considerably greater than one have been obtained in nanostructured lead-based materials, such as $(PbTe)_m$-$AgSbTe_2$ systems [6–13]. Because of the strict environmental regulations anticipated for the use of these systems, new compounds, such as lead-free p-type $AgSn_mSbTe_{2+m}$, n-type $AgBiSe_2$, $BiAgSeS$, GeTe-doped $AgSbTe_2$ (TAGS), $Ag_{0.85}SnSb_{1.15}Te_3$ and $BiSbSTe_2$, may constitute attractive alternatives [15–22]. Chalcogenides, such as p-type $(SnTe)_m$-$AgSbTe_2$ and $(SnTe)_m$-$AgBiTe_2$ systems, have recently been proposed as alternatives to lead-based materials because of their high thermoelectric properties. These chalcogenides exhibit low thermal conductivities and large positive Seebeck coefficients. Some investigations of the thermoelectric properties of $(SnTe)_m$-$AgBiTe_2$ systems have revealed a remarkably low thermal conductivity (κ) [23]. For example, the obtained κ was $\sim 0.6\,W\,m^{-1}\,K^{-1}$, and the peak ZT value was approximately 1.1 at ~ 775 K.

One aspect that has not been developed is the preparation of new lead-free $(SnTe)_m$-$AgSbSe_2$ systems. The experimental results showed that an anion isovalent chemical substitution (Te is replaced by Se) causes a decrease of the thermal conductivity and increase of the powder factor ($S^2\sigma$) [24,25]. For example, chemical substitution of Se by Te in LAST-18 ($AgPb_{18}SbSe_2Te_{18}$) resulted in a material with a κ_{latt} of $\sim 0.78\,W\,m^{-1}\,K^{-1}$, which is half of the value for $AgPb_{18}SbTe_{20}$. In this work, we report the synthesis, characterization and electrical properties of new $AgSn_mSbSe_2Te_m$ systems obtained via the isomorphic substitution of a fraction of the Te by Se. We successfully synthesized $AgSn_mSbSe_2Te_m$ ($m = 2$ and 10) at high temperatures using solid-state reactions. The parallelepiped bars used for transport measurements were prepared from melted samples and by spark plasma sintering (SPS). $AgSn_mSbSe_2Te_m$ ($m = 10$) exhibited a lattice thermal conductivity (κ_{latt} of $\sim 0.6\,W\,m^{-1}\,K^{-1}$. The Seebeck coefficient for p-type $AgSn_2SbSe_2Te_2$ was $\sim +70\,\mu V\,K^{-1}$ (SPS). These materials showed ZT values of ~ 0.10 at room temperature.

2. Experimental section

2.1. Synthesis

$AgSn_mSbSe_2Te_m$ were synthesized using Ag powder (99.99%, ALDRICH), Sn powder (99.9+%, ALDRICH), Sb powder (99.99%, ALDRICH), Se powder (99.99+%, ALDRICH) and Te powder (99.9%, ALDRICH) in stoichiometric amounts (~2.0 g of compound). The stoichiometric mixtures were placed into dried quartz tubes under an argon atmosphere. These quartz tubes were evacuated and flame-sealed under an argon atmosphere. The reaction ampoules were slowly heated at $150\,°C\,h^{-1}$ to 1223 K (950 °C) and maintained at this temperature for 16 h. The furnace was cooled to room temperature at $\sim 50\,°C\,h^{-1}$. Two methods were used to obtain suitable parallelepiped-shaped samples for electrical measurements. In method 1, the classical method (CM), the obtained samples were crushed into powders and placed into a quartz cell with a parallelepiped shape. This quartz cell was placed into a larger quartz tube, which was evacuated and flame-sealed under an argon atmosphere. The quartz tube was used to prevent oxidation of the pellets by air. This tube was then placed into a furnace at 750 °C for ~4 min and then quickly removed from the furnace. The obtained ingots were cut and polished for measurements of their electrical transport and thermal properties. Method 2 was SPS. The selected fine powders were densified using SPS (SPS-511S, Dr. Sinter) in a ⌀10 mm graphite mold under flowing argon. Many different experimental conditions were used, with the pressures varied between 75 MPa and 150 MPa and the temperatures varied between 750 K and 800 K. However, most of the pellets contained cracks, and very few of them did not break. In addition, all of them were very brittle. They were suitable for thermal diffusivity, low-temperature Seebeck coefficient and electrical conductivity measurements; however, parallelepiped-shaped samples suitable for Seebeck measurements at high temperatures could not be prepared. The bars were too brittle and broke when clamped into the measurement system.

2.2. Structural characterization and chemical analyses

Powder X-ray diffraction (PXRD) patterns were collected at room temperature on a Bruker D8 Advance diffractometer equipped with a Cu Kα radiation source. Samples were scanned in the range $5° < 2\theta < 80$. XRD patterns were refined by the Rietveld method using the MAUD software. A standard LaB_6 sample was used for measuring the instrumental profile.

The chemical compositions of the samples were determined by energy-dispersive X-ray spectroscopy (EDS) in conjunction with scanning electron microscopy (SEM) carried out on a Bruker Vega 3 Tescan system equipped with Quantax 400 (EDS) microanalyzer. Samples were mounted onto double-sided carbon tape, which was adhered to an aluminum specimen holder. High-resolution transmission electron microscopy (HRTEM) and electron diffraction (ED) patterns were obtained using a JEOL JEM 3000F operating at an accelerating voltage of 300 kV. Samples were prepared by crushing the powders under n-butanol and dispersing them over copper grids covered with a holey carbon film. Semi-quantitative chemical analyses were carried out using EDS. L-edges were considered for Ag, Sn, Sb and Te atoms, whereas the K-edge was chosen for Se.

Differential scanning calorimetry (DSC) and thermogravimetric analysis (TG) were performed on a Rheometric Scientific STA 1500H/625 thermal analysis system. DSC/TG curves were acquired simultaneously for each sample over the temperature range from room temperature to 1000 °C; the samples were heated at 10 °C min^{-1} under flowing argon at a heating rate of. DSC/TGA heating/cooling experiments were conducted in argon atmosphere.

2.3. Electrical and thermal properties

Samples were cut into rectangular shapes of ~3 mm × 3 mm × 9 mm. Hall-effect measurements were obtained in a PPMS environment from 20 K to 300 K using a Keithley 6220 current source and a Keithley 2182A nanovoltmeter. The Hall-effect measurements from 300 K to 450 K were obtained using an ECOPIA HMS 2000 system (Van der Pauw method). The low-temperature Seebeck coefficient S and the electrical conductivity σ were measured simultaneously by using a laboratory made system in a He-free cryostat from 20 K to room temperature (R.T.). The thermal conductivity was calculated from $\kappa = D \cdot C_p \cdot \rho$, where the thermal diffusivity coefficient (D) was measured using the laser flash diffusivity method in a Netzsch LFA 427. The samples obtained as ingots were cut and polished into a parallelepiped shapes with dimensions of $8 \times 8 \times$ ~1.5–2.0 mm^3 for the thermal diffusivity measurements. The density (ρ) was determined using the dimensions and mass of the samples and was approximately 92–96% of the theoretical value. The specific heat capacity (C_p) values were determined by calorimetric measurements using a TA Instruments Discovery DSC calorimeter. Experiments were carried out from R.T. to 500 °C at 10 °C min^{-1} under N$_2$. Sample and sapphire cells were measured in quadruplicate. The C_p measurements show good agreement with the value estimated from Dulong-Petit Law: $C_p = 3R/M$, where R is the ideal gas constant and M is the average relative atomic mass.

3. Results and discussion

3.1. X-ray powder diffraction, thermal and compositional characterization

PXRD patterns and SEM-EDS analysis indicate that the reaction products of the nominal composition AgSn$_m$SbSe$_x$Te$_{m-x}$ ($x > 2$) are not single phases. For example, the reaction products of the nominal compositions AgSn$_4$SbSe$_3$Te$_3$ and AgSn$_{10}$SbSe$_6$Te$_6$ are composed of AgSn$_m$SbTe$_m$, Ag$_2$Te, SnTe (~20% of binary compounds) and some unidentified impurities (Fig. S1- Supplementary material). In the cases of AgSn$_m$SbSe$_2$Te$_m$ ($m = 4$, 16 and 18), the diffraction peaks can be indexed to the $Pm\overline{3}m$ space group (distorted NaCl-type structure), with the exception of two very weak peaks (Fig. S2). The PXRD patterns show a very small amount of Ag$_2$Te impurities. The backscattered image and EDS analysis (elemental maps) revealed that the samples with nominal compositions of AgSn$_m$SbSe$_2$Te$_m$ ($m = 2$ and 10) are uniform throughout the scanned region (Figs. S3–S4). The AgSn$_m$SbSe$_2$Te$_m$ ($m = 2$, 4, 10, 16 and 18) systems appear to congruently melt at ~607, ~635, ~671, ~714 and ~719 °C, respectively (Fig. S5). A comparison of the PXRD patterns collected before and after the DSC/TG analyses showed no significant changes.

Fig. 1 presents the PXRD patterns and the lattice parameters for the AgSn$_m$SbSe$_2$Te$_m$ samples. Fig. 2 shows a representative Rietveld PXRD pattern of AgSn$_{10}$SbSe$_2$Te$_{10}$. In this work, the lattice parameters change monotonically as a function of m (Fig. 1b). The change in the crystallographic anion or cation site preference must affect the lattice parameters. In these systems, there is no evidence of immiscibility and the lattice parameters range between the lattice parameter of AgSbSe$_2$ (5.788 Å) and that of SnTe (6.309 Å). The AgSn$_m$SbSe$_2$Te$_m$ family of compounds cannot be viewed simply as solid solutions but instead as a (AgSbSe$_2$)-(SnTe)$_m$ system. The inset in Fig. 2 displays lattice parameters as a function of AgSbSe$_2$%, which was calculated from the $1/(1 + m)$ molar ratio. The lattice parameters plotted against AgSbSe$_2$% show linear behavior; this behavior has previously been observed in AgSn$_x$BiTe$_{x+2}$ and LAST-m systems (i.e., AgPb$_m$SbTe$_{m+2}$) [18,23].
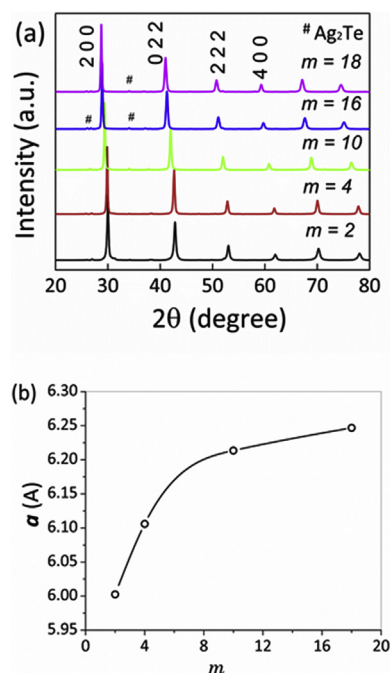

Fig. 1. (a) PXRD pattern of AgSn$_m$SbSe$_2$Te$_m$ and (b) plot of lattice a parameters against m.

3.2. HRTEM analyses

The microstructural features of the prepared samples were analyzed using HRTEM. Small polycrystals with no polygonal shape and slightly rough borders were observed, consistent with the milling process. Mean atomic compositions similar to the expected compositions were obtained: Ag$_{1.0}$Sn$_{2.4}$Sb$_{1.0}$Se$_{2.3}$Te$_{2.3}$ and Ag$_{1.4}$Sn$_{9.6}$Sb$_{0.9}$Se$_{2.1}$Te$_{10}$ for $m = 2$ and $m = 10$ (AgSn$_m$SbSe$_2$Te$_m$), respectively. Fig. 3a, Fig. 3b and Fig. S6 (Supplementary material) present typical crystals with jagged edges and a crease-type appearance that does not generate extra spots in the ED patterns obtained for different selected regions. These formations that endotaxially match the matrix, without clear borders, are probably related to chemical segregation with respect to the Ag and Sb contents, which is also observed in LAST-m systems. Well-delimited nanoprecipitates previously reported in similar systems were not detected in our case (see Fig. 3c) [20]. The crystals of $m = 10$ are smaller and more clearly constructed from the aggregation of nanocrystals, as revealed by the very close semicircles in the fast Fourier transforms (FFTs) (see Fig. 3d). A systematic inspection revealed the existence of different types of inhomogeneities at the nanoscale, which are known to greatly influence the thermoelectrical response of the materials [26,27]. In addition, high densities of dislocations and imperfections are present in our samples (Fig. S7).

The presence of different contrast zones was detected in the sample crystals, and these zones were observed to a greater extent, as shown in Fig. 4. These zones can be interpreted as nanoregions of different crystallinity that coexist throughout the crystal bulk, as previously detected in other chalcogenides [28]. This microstructural characteristic can be linked to the mechanical fragility displayed in these materials. In addition, nanoregions with different orientations or symmetries were detected. In Fig. 5a, the coexistence of [100] and [110] zone axes can be observed, whereas the presence of [110] and [111]-oriented nanodomains or tetragonal nanoregions was detected in other cases (Figs. S6 and S8). Streaking

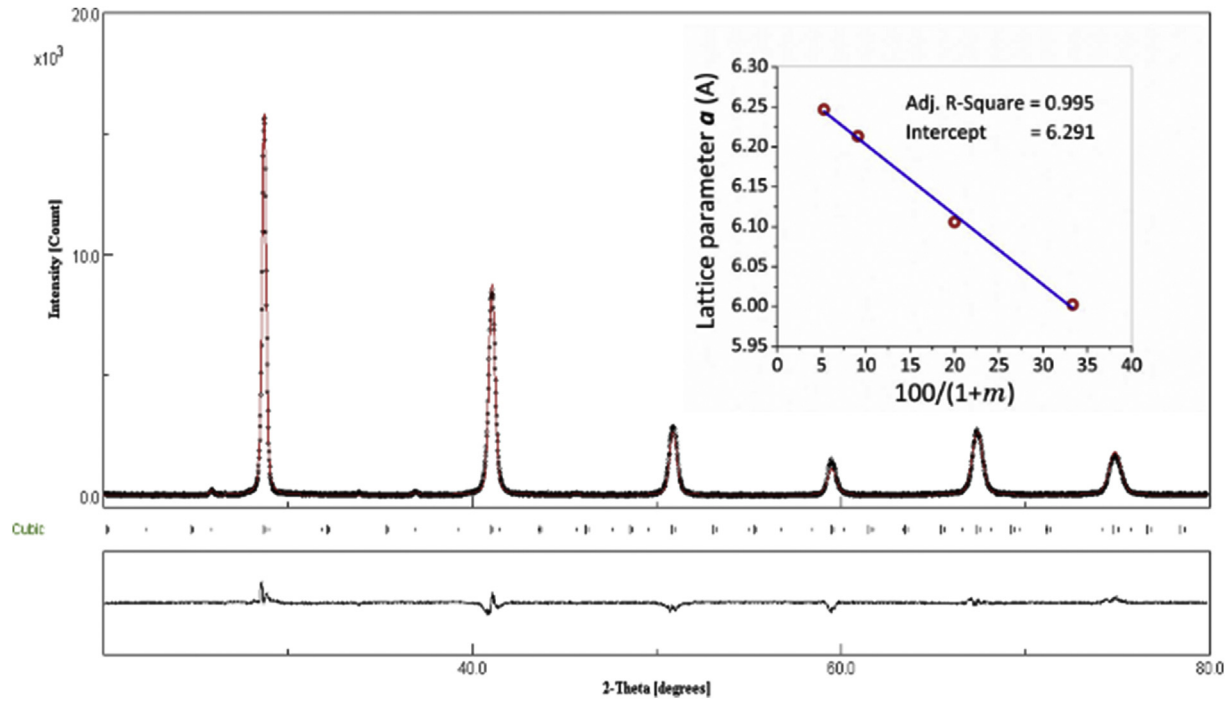**Fig. 2.** Final Rietveld refinement plot of $AgSn_{10}SbSe_2Te_{10}$. Observed (open circles), calculated (line) and difference X-ray diffraction profiles are plotted. The insert shows cell a parameters as a function of $AgSbSe_2$ molar %, $100/(1 + m)$.
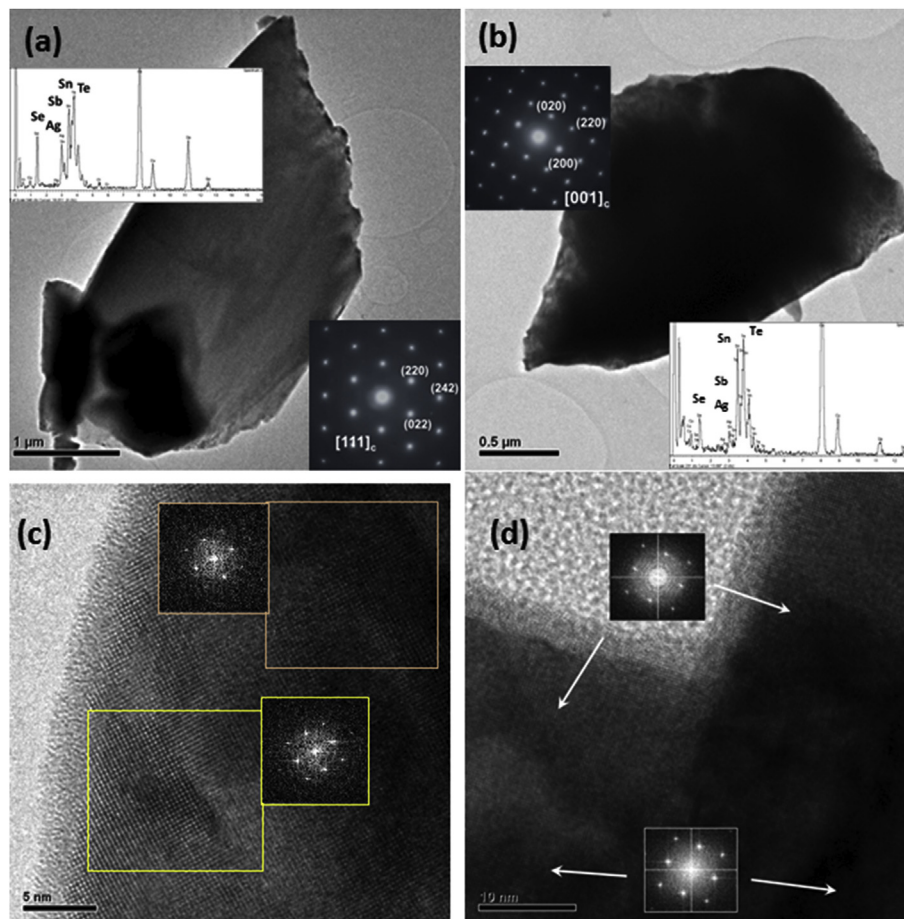

Fig. 3. HRTEM images showing EDX spectra and ED patterns for $AgSn_2SbSe_2Te_2$ (a) and $AgSn_{10}SbSe_2Te_{10}$ (b). HRTEM images showing fast fourier transforms (FFTs) and chemical compositions for $AgSn_2SbSe_2Te_2$ (c) and $AgSn_{10}SbSe_2Te_{10}$ (d) obtained for different selected regions.

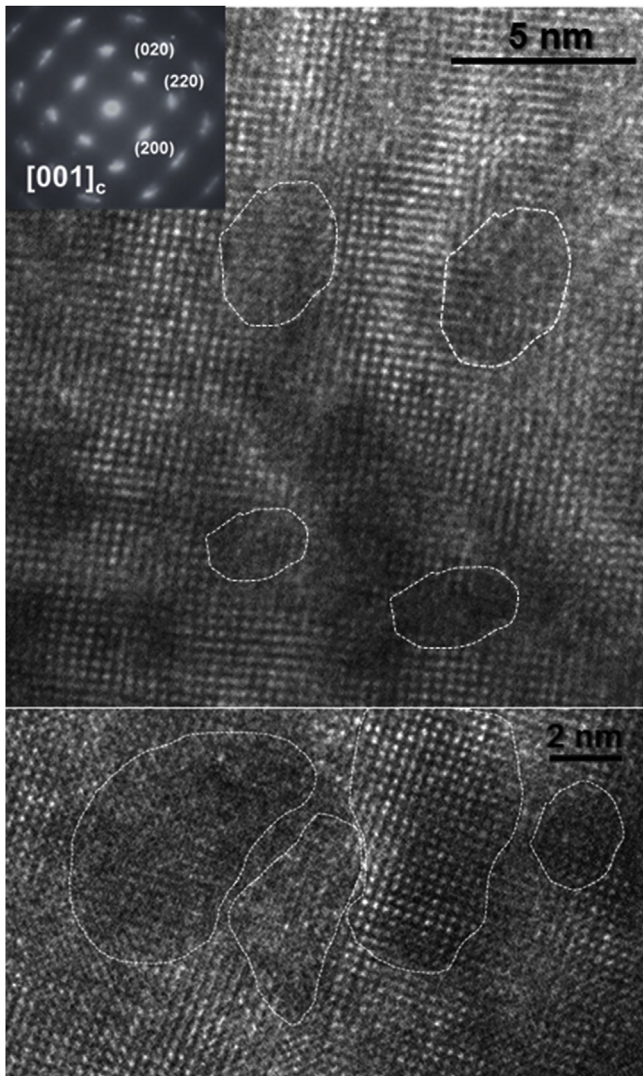**Fig. 4.** HRTEM images with different contrast zones of AgSn$_{10}$SbSe$_2$Te$_{10}$ that show nanoregions with different crystallinity (roughly marked by discontinuous white lines).

is observed, especially for $m = 10$, which is consistent with high atomic disorder (Fig. 5b). However, short-range atomic ordering, which causes extra spots or satellite reflections, was observed in some cases, similar to the short-range atomic ordering in the previously analyzed parent systems [29].

3.3. Thermoelectric properties

Fig. 6 shows the temperature dependence of the electrical conductivity (σ) and Seebeck coefficient (S) for the parallelepipeds of AgSn$_m$SbSe$_2$Te$_m$ ($m = 2$ and 10). The σ decreased almost linearly with increasing temperature (78–300 K). As shown, compounds with $m = 2$ and 10 prepared by CM method exhibit electrical conductivities of ~1490 and ~3200 S cm^{-1} at R.T., respectively, which are similar to those of AgSn$_m$SbTe$_{m+2}$ (1800 S cm^{-1} for $m = 2$ and 2800 S cm^{-1} for $m = 10$) [18]. The electrical conductivities σ for the samples prepared using SPS were ~492 S cm^{-1} and ~1620 S cm^{-1} ($m = 2$ and $m = 10$, respectively). The values of σ for the samples prepared using SPS were approximately half the values
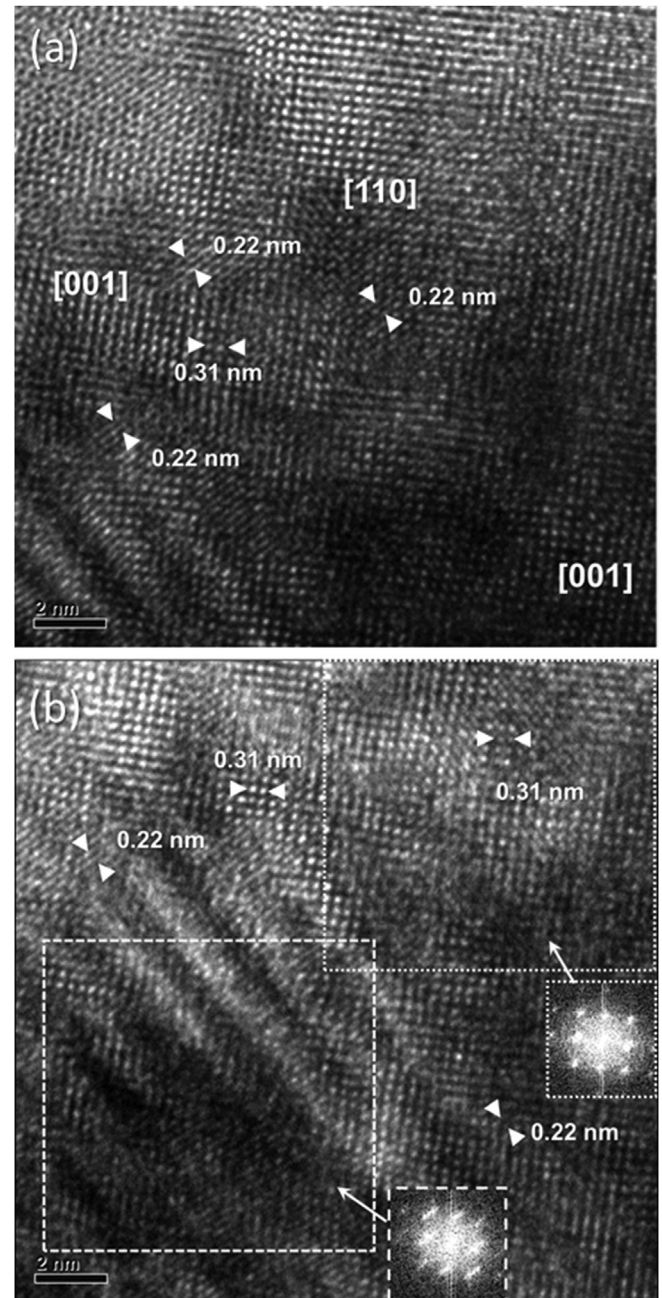

Fig. 5. HRTEM images for AgSn$_{10}$SbSe$_2$Te$_{10}$ revealing nanoregions with different orientations (a) and corresponding FFTs (b). The white superimposed on the images indicates the interplanar distances.

of σ for the samples prepared using CM. The positive values of the Seebeck coefficient indicate that the transport properties are dominated by holes. The positive values of S are consistent with the results of the Hall measurements (see below). The measured Seebeck coefficient is low, approximately +35 μV K^{-1} at 300 K, and steadily increases with increasing temperature. This value is approximately two times lower than the values of AgSn$_m$SbTe$_{m+2}$ systems and compares very well with SnTe, approximately +40 μV K^{-1} at 300 K. A power factor of $S^2\sigma$ ~2.0 μW cm^{-1} K^{-2} was obtained at 300 K. The power factors in AgSn$_m$SbTe$_{m+2}$ are 5–12 μW cm^{-1} K^{-2} at 300 K [18]. However, the
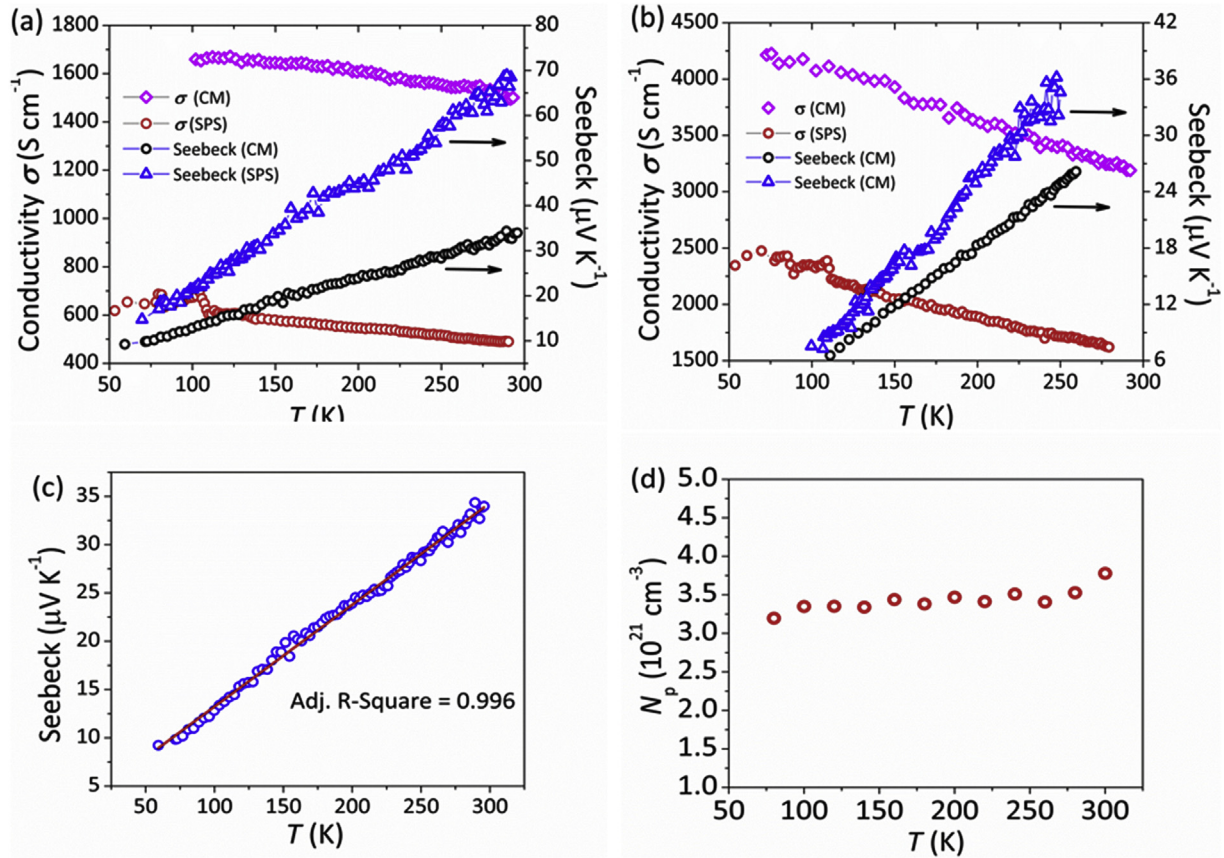
Fig. 6. The electrical conductivity σ and Seebeck coefficients as a function of temperature for AgSn$_2$SbSe$_2$Te$_2$ (a) and AgSn$_{10}$SbSe$_2$Te$_{10}$ (b) prepared by CM and SPS. (c) A representative linear plot of the Seebeck coefficient S versus temperature for AgSn$_2$SbSe$_2$Te$_2$ and the carrier concentration as a function of temperature for AgSn$_{10}$SbSe$_2$Te$_{10}$ (d).

Seebeck coefficients of the AgSn$_2$SbSe$_2$Te$_2$ sample prepared using SPS are larger than those of the melted samples prepared using CM (Fig. 6). The Seebeck coefficients for the prepared samples using SPS were approximately +70 μV K^{-1} (m = 2) and approximately +40 μV K^{-1} (m = 10) at 300 K. A power factor of S^{2}σ ~22 μW cm^{-1} K^{-2} (SPS) was obtained for m = 2 at 300 K, which is approximately ten times larger than the value obtained for the samples prepared using CM. It means that the concentration of electroactive defects is dependent on the synthesis process. Indeed, both methods can be described as "out-of-equilibrium", with different thermal processes that should lead to different concentration or distribution of defects. This finding indicates that the synthesis and densification process strongly influences the defect chemistry of these materials and, therefore, their electrical transport properties.

The Hall coefficients are positive in the temperature range studied, which is indicative of p-type behavior. Fig. 6d shows the hole concentrations as a function of temperature for AgSn$_{10}$Sb-Se$_2$Te$_{10}$. The hole concentrations were almost constant until ~300 K, with a carrier concentration of ~3.5 × 10^{21} cm^{-3}. Kanatzidis et al. reported values of ~5 × 10^{21} cm^{-3} for Ag$_{0.85}$SnSb$_{1.15}$Te$_3$ [17]. The hole mobility is not particularly high: approximately 5.0–8.0 cm^2 V^{-1} S^{-1} between 78 and 300 K. The AgSn$_m$SbTe$_{m+2}$ systems showed carrier mobilities between 120 and 30 cm^2 V^{-1} S^{-1}. These materials show typical degenerate semiconductor behavior. These results are consistent with the behavior previously reported for AgSn$_x$BiTe$_{x+2}$ and can be attributed to the high carrier concentration [23].

The temperature dependence relationship of the Seebeck coefficient for degenerate semiconductors is given by

$$S = \left[\frac{8\pi^{2/3}k_B^2(r+3/2)}{3^{5/3}eh^2}\right]\left(\frac{m^*}{n^{2/3}}\right)T \quad (1)$$

where S is the Seebeck coefficient, m* is the effective mass, k$_B$ is Boltzmann's constant, e is the charge of an electron, h is Planck's constant, and n is the carrier concentration. The Seebeck coefficient was fit in the corresponding temperature range of 78 K ≤ T ≤ 300 K, from which the effective mass (m*) was obtained. Fig. 6c shows a representative plot for AgSn$_{10}$SbSe$_2$Te$_{10}$. The Seebeck measurements for AgSn$_{10}$SbSe$_2$Te$_{10}$ imply a large m* ~4.7 m$_0$ with an acoustic phonon scattering mechanism (r = −1/2) and m* ~ 1.6 m$_0$ with an ionized impurity scattering mechanism (r = 3/2), respectively. AgSn$_2$SbSe$_2$Te$_2$ exhibits m* ~3.4 m$_0$, with and acoustic phonon scattering mechanism (r = −1/2) and m* ~1.2 m$_0$ with an ionized impurity scattering mechanism (r = 3/2), respectively. Large effective masses, m* ~6 m$_0$, have been observed in Ag$_{0.85}$SnSb$_{1.15}$Te$_3$ [18]. A plot of the Seebeck coefficient against lnσ exhibits linear behavior (Fig. S9). The slope was ~65 μV K^{-1}, which is larger than the classical value of 0.73 μV K^{-1} (∂S/∂lnσ ~ k$_B$/e). This behavior at high temperature has been observed in other thermoelectric systems, such as Ag(Pb$_{1-y}$Sn$_y$)$_m$SbTe$_{m+2}$ [30].

The temperature dependence total thermal conductivity (κ$_{tot}$) and electrical conductivity at high temperatures for AgSn$_{10}$Sb-Se$_2$Te$_{10}$ is shown in Fig. 7. The temperature dependence of the thermal diffusivity is shown in Fig. S10. The electrical conductivity (σ) decreased almost linearly with increasing temperature (Fig. 7a). The κ$_{tot}$ values are ~3.0 W m^{-1}K^{-1} at 300 K and ~2.5 W m^{-1} K^{-1} at 900 K. These values are comparable to the values of κ$_{tot}$ in
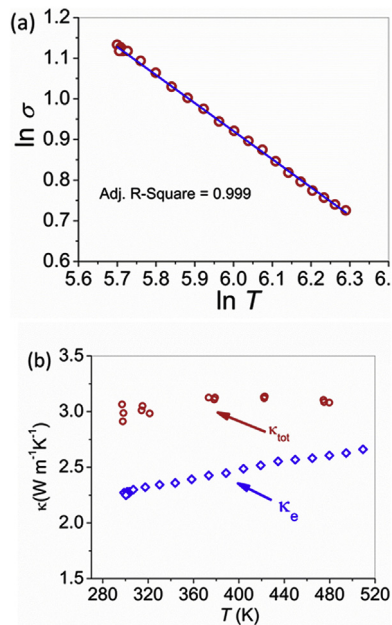
Fig. 7. Plot of the natural logarithm of the electrical conductivity σ versus the natural logarithm of the temperature (a) and thermal conductivity κ_{tot} and electron thermal conductivity κ_e as a function of temperature (b) for $AgSn_{10}SbSe_2Te_{10}$ prepared by CM method.

$AgSn_{25}SbTe_{27}$, which are ~3.4 W m^{-1}K^{-1} at 300 K and ~2.2 W m^{-1}K^{-1} at 800 K [23]. The electron thermal conductivity (κ_e) was calculated using the Wiedemann-Franz relationship:

$$\kappa_e = L\,\sigma\,T \qquad (2)$$

where T is the absolute temperature, σ is the electrical conductivity, and L is the Lorenz number, which is $L = \pi^2 k_B^2/3e^2 = 2.45 \times 10^{-8}$ W Ω K^{-2}. The value of the Lorenz number depends on the carrier concentration. In our case of degenerate semiconductor behavior, this value is a very good approximation. Our results indicate that the κ_e is the most important contribution to κ_{tot} at high temperatures (T > 450 °C). The lattice thermal conductivity (κ_{latt}) decreases with an increase temperature ($\kappa_{latt} = \kappa_{tot} - \kappa_e$). The κ_{latt} value of $AgSn_{10}SbSe_2Te_{10}$ at 300 K is ~0.6 Wm^{-1}K^{-1}, which is comparable to the κ_{latt} of $AgPb_{12}Sn_4Sb_{0.4}Te_{20}$ (~0.7 Wm^{-1}K^{-1}) [30].

4. Conclusions

$AgSn_mSbSe_2Te_m$ ($m = 2$ and 10) systems were successfully prepared at high temperatures using solid-state reactions. HRTEM revealed the existence of different types of inhomogeneities at the nanoscale and nanoregions of different crystallinity. This microstructural characteristic can be linked to the mechanical fragility exhibited by the materials. The transport properties of *p*-type $AgSn_mSbSe_2Te_m$ systems exhibit typical degenerate semiconductor behavior. The Seebeck coefficient can be increased from ~+40 μV K^{-1} (CM) to ~+70 μV K^{-1} (SPS) in $AgSn_2SbSe_2Te_2$ at room temperature ($S^2\sigma$ ~ 22 μW cm^{-1} K^{-2}). On the basis of the electrical and thermal transport properties, *ZT* values of ~0.10 were obtained at room temperature.

Acknowledgements

Appendix A. Supplementary data

Supplementary data related to this article can be found at https://doi.org/10.1016/j.matchemphys.2018.02.047.

References

[1] X. Zhang, L.-D. Zhao, Thermoelectric materials: energy conversion between heat and electricity, J. of Materiomics 2 (2015) 92—105.
[2] A.J. Minnich, M.S. Dresselhaus, Z.F. Ren, G. Chen, Bulk nanostructured thermoelectric materials: current research and future prospects, Energy Environ. Sci. 2 (2009) 466—479.
[3] J.R. Sootsman, D.Y. Chung, M.G. Kanatzidis, New and old concepts in thermoelectric materials, Angew. Chem. Int 48 (2009) 8616—8639.
[4] M.G. Kanatzidis, Nanostructured thermoelectrics: the new paradigm? Chem. Mater. 22 (2010) 648—659.
[5] C.J. Vineis, A. Shakouri, A. Majumdar, M.G. Kanatzidis, Nanostructured thermoelectrics: big efficiency gains from small features, Adv. Mater. 22 (2010) 3970—3980.
[6] D.I. Bilic, S.D. Mahanti, M.G. Kanatzidis, Electronic transport properties of PbTe and $AgPb_mSbTe_{2+m}$ systems, Phys. Rev. B 74 (2006) 125202.
[7] K.-F. Hsu, S.F. Loo, Guo, W. Chen, J.S. Dyck, C. Uher, T. Hogan, E.K. Polychroniadis, M.G. Kanatzidis, Cubic $AgPb_mSbTe_{2+m}$: bulk thermoelectric materials with high figure of merit, Science 303 (2004) 818—821.
[8] E. Quarez, K.-F. Hsu, R. Pcionek, N. Frangis, E.K. Polychroniadis, M.G. Kanatzidis, Nanostructuring, compositional fluctuations, and atomic ordering in the thermoelectric materials AgPbmSbTe2+m.The myth of solid solutions, J. Am. Chem. Soc. 127 (2005) 9177—9190.
[9] D. Bilic, S.D. Mahanti, E. Quarez, K.-F. Hsu, R. Pcionek, M.G. Kanatzidis, Resonant states in the electronic structure of the high performance thermoelectrics $AgPb_mSbTe_{2+m}$: the role of Ag-Sb microstructures, Phys. Rev. Lett. 93 (2004) 146403.
[10] H. Lin, S. Božin, S.J.L. Billinge, E. Quarez, M.G. Kanatzidis, Nanoscale clusters in the high performance thermoelectric $AgPb_mSbTe_{m+2}$, Phys. Rev. B 72 (2005) 174113.
[11] A. Kosuga, M. Uno, K. Kurosaki, S. Yamanaka, Thermoelectric properties of stoichiometric $Ag_{1-x}Pb_{18}SbTe_{20}$ (x = 0, 0.1, 0.2), J. Alloy. Comp. 391 (2005) 288—291.
[12] M.K. Han, K. Hoang, H. Kong, R. Pcionek, C. Uher, K.M. Paraskevopoulos, S.D. Mahanti, M.G. Kanatzidis, Substitution of Bi for Sb and its role in the thermoelectric properties and nanostructuring in $Ag_{1-x}Pb_{18}MTe_{20}$(M = Bi, Sb) (x = 0, 0.14, 0.3), Chem. Mater. 20 (2008) 3512—3520.
[13] I. Arachchige, J. Wu, V.P. Dravid, M.G. Kanatzidis, Nanocrystals of the quaternary thermoelectric materials: AgPbmSbTem+2 (m=1—18): phase-segregated or solid solutions? Adv. Mater. 20 (2008) 3638—3642.
[14] P.F.P. Poudeu, J. D'Angelo, A.D. Downey, J.L. Short, T.P. Hogan, M.G. Kanatzidis, High thermoelectric figure of merit and nanostructuring in bulk p-type $Na_{1-x}Pb_mSb_yTe_{m+2}$, Angew. Chem. Int. Ed. 45 (2006) 3835—3839.
[15] J.H. Kim, D.Y. Chung, D. Bilc, S. Loo, J. Short, S.D. Mahanti, T. Hogan, M.G. Kanatzidis, Crystal growth, thermoelectric properties, and electronic structure of AgBi3S5 and AgSbxBi3-xs5(x = 0.3), Chem. Mater. 17 (2005) 3606—3614.
[16] J.R. Salvador, J. Yang, X. Shib, H. Wang, A.A. Wereszczak, Transport and mechanical property evaluation of $(AgSbTe)_{1-x}(GeTe)_x$ (x = 0.80, 0.82, 0.85, 0.87, 0.90), J. Solid State Chem. 182 (2009) 2088—2095.
[17] J. Androulakis, R. Pcionek, E. Quarez, J-H. Do, H. Kong, O. Palchik, C. Uher, J.J. D'Angelo, J. Short, T. Hogan, M.G. Kanatzidis, Coexistence of large thermopower and degenerate doping in the nanostructured material $Ag_{0.85}SnSb_{1.15}Te_3$, Chem. Mater. 18 (2006) 4719—4721.
[18] M.K. Han, J. Androulakis, S.J. Kim, M.G. Kanatzidis, Lead-free thermoelectrics: high figure of merit in p-type $AgSn_mSbTe_{m+2}$, Adv. Energy Mater 2 (2012) 157—161.
[19] L. Pan, D. Bérardan, N. Drago, High thermoelectric properties of n-type AgBiSe2, J. Am. Chem. Soc. 135 (2013) 4914—4917.
[20] Y.-L. Pei, H. Wu, J. Sui, J. Li, D. Berardan, C. Barreteau, L. Pan, N. Drago, W.-S. Liu, J. He, L.-D. Zhao, High thermoelectric performance in n-type BiAgSeS due to intrinsically low thermal conductivity, Energy Environ. Sci. 6 (2013) 1750—1755.
[21] S.N. Guin, A. Chatterjee, D. Singh Negi, R. Datta, K. Biswas, High thermoelectric performance in tellurium free p-type AgSbSe2, Energy Environ. Sci. 6 (2013) 2603—2608.
[22] R. Mohanraman, R. Sankar, F.C. Chou, C.H. Lee, Y.-Y. Chen, Enhanced thermoelectric performance in Bi-doped p-type AgSbTe2 compounds, J. Appl. Phys. 114 (2013) 163712.
[23] G. Tan, V.P. Dravid, F. Shi, L.D. Zhao, M.G. Kanatzidis, SnTe—AgBiTe2 as an efficient thermoelectric material with low thermal conductivity, J. Mater. Chem. A 2 (2014) 20849—20854.
[24] H. Li, Y. Du, H.F. Wang, S.Z. Shen, X.L. Li, Y.Y. Wang, C.W. Zhou, Preparation and thermoelectric properties of $AgPb_{18}SbTe_{20-x}Se_x$ (x = 1, 2, 4) materials, Curr. Appl. Phys. 12 (2012) 188—192.
[25] K.F. Cai, X.R. He, M. Avdeev, D.H. Yu, J.L. Cui, H. Li, Preparation and thermoelectric properties of $AgPb_mSbSe_{m+2}$ materials, J. Solid State Chem. 181 (2008) 1434—1438.

[26] Q. Jiang, J. Yang, Y. Liu, H. He, Microstructure tailoring in nanostructured thermoelectric materials, J. Adv. Dielectrics 6 (2016) 1630002.

[27] S. Bathula, M. Jayasimhadri, B. Gahtori, N. Kumar Singh, K. Tyagi, A.K. Srivastava, A. Dhar, The role of nanoscale defect features in enhancing the thermoelectric performance of p-type nanostructured SiGe alloys, Nanoscale 7 (2015) 12474–12483.

[28] S. Bhattacharya, A. Bohra, R. Basu, R. Bhatt, S. Ahmad, K.N. Meshram, A.K. Debnath, A. Singh, S.K. Sarkar, M. Navneethan, Y. Hayakawwa, D.K. Aswal, S.K. Gupta, High thermoelectric performance of $(AgCrSe_2)_{0.5}(CuCrSe_2)_{0.5}$ nano-composites having all-scale natural hierarchical architectures, J. Mater. Chem. A2 (2014) 17122–17129.

[29] O. Falkenbach, A. Schmitz, T. Dankwort, G. Koch, L. Kienle, E. Muller, S. Schelecht, Tin telluride-based nanocomposites of the type $AgSn_mBiTe_{2+m}$ (BTST-m) as effective lead-free thermoelectric materials, Chem. Mater. 27 (2015) 7296–7305.

[30] J. Androulakis, K.F. Hsu, R. Pcionek, H. Kong, C. Uher, J.J. D'Angelo, A. Downey, T. Hogan, M.G. Kanatzidis, Nanostructuring, High Thermoelectric, Efficiency in p-Type $Ag(Pb_{1-y}Sny)mSbTe_{2+m}$, Adv. Mater. 18 (2006) 1170–1173.